Journal of
Materials Chemistry C

ROYAL SOCIETY
OF CHEMISTRY

PAPER

View Article Online
View Journal

Cite this: DOI: 10.1039/c9tc05550a

An excited state managing molecular design platform of blue thermally activated delayed fluorescence emitters by π-linker engineering†

Kyung Hyung Lee,‡[a] Soon Ok Jeon, ‡*[b] Yeon Sook Chung,[b] Masaki Numata,[c] Hasup Lee,[b] Eun Kyung Lee, [b] Eun Suk Kwon,[b] Myungsun Sim,[b] Hyeonho Choi [b] and Jun Yeob Lee *[a]

Received 10th October 2019,
Accepted 11th December 2019

DOI: 10.1039/c9tc05550a

rsc.li/materials-c

A molecular design platform of blue thermally activated delayed fluorescence (TADF) emitters to boost the external quantum efficiency and efficiency roll-off of blue TADF organic light-emitting diodes (OLEDs) was developed. A molecular structure hiring one or two excited state controlling subunits in the π-linker between a donor and an acceptor was employed. The subunit in the π-linker was a phenyl unit to precisely control the performances of TADF devices. It was described that the phenyl subunit simultaneously improved the external quantum efficiency and efficiency roll-off of TADF OLEDs. A high external quantum efficiency of 28.5% was demonstrated using the material design having two phenyl sub units.

Introduction

Since the first demonstration of close to 20% external quantum efficiency (EQE) using a thermally activated delayed fluorescence (TADF) emitter, the progress of the TADF device characteristics has been surprisingly remarkable. The EQE of TADF organic light-emitting diodes (OLEDs) was even further enhanced from 20% to close to 30% in the red device and even over 30% in the green and blue devices by developing several material design platforms of TADF emitters.[1–17]

The most popular material design platform of TADF emitters is the donor-π linker-acceptor structure. The donor and acceptor parts in the TADF structure mainly govern the charge transfer (CT) characteristics related with the singlet and triplet energies, and the π-linker part dominates the orbital overlap for efficient light emission. In many research studies, donor and acceptor engineering was the main approach to manage the TADF performances of TADF emitters because the key process of reverse intersystem crossing (RISC) was mostly determined by the donor and the acceptor.[18] A π-linker engineering has been a minor part in the TADF material design.[19] However, the importance of the π-linker has been described in several publications in recent years.[20–22] Although the main role of the π-linker is to control the orbital overlap for radiative transition, it can also affect the RISC by strengthening or weakening the CT properties of TADF emitters. For instance, the introduction of a methyl group or a CN group into the π-linker controlled the emission energy and RISC properties of TADF emitters.[23,24]

Herein, we describe a molecular design platform of blue TADF emitters for high EQE and improved efficiency roll-off. A π-linker engineering approach through phenyl subunits was employed to reduce the singlet–triplet energy gap (ΔE_{ST}) for an efficient RISC process. It was demonstrated that the molecular design platform adopting phenyl subunits in the π-linker facilitated the RISC process and enhanced the EQE of TADF OLEDs. Moreover, the supplementary reduction of the efficiency roll-off was proven by π-linker engineering. A high EQE of 28.5% was demonstrated using a TADF material with two phenyl subunits in the π-linker.

Results and discussion

A π-linker modifying approach was adopted to establish a molecular design platform of highly efficient blue TADF emitters. The motivation for π-linker engineering is that the aromatic linker can control the excited state of TADF emitters by electronic communication and spatial management of the molecular structure. One or two phenyl subunits were introduced into the phenyl linker at the *ortho* position to the donor substitution position to manage the excited state through the donor geometry control. We selected **CTrz** as a standard blue TADF material because of its promising property reported in previous work.[25]

---

[a] *School of Chemical Engineering, Sungkyunkwan University 2066, Seobu-ro, Jangan-gu, Suwon, Gyeonggi, 16419, Korea. E-mail: leej17@skku.edu*

[b] *Samsung Advanced Institute of Technology, Samsung Electronics Co., Ltd, 130 Samsung-ro, Suwon-si, Gyeonggi-do 16678, Korea. E-mail: so.jeon@samsung.com*

[c] *Samsung R&D Institute Japan, 2-7 Sugasawa-cho, Tsurumi-ku, Yokohama, Japan*

† Electronic supplementary information (ESI) available. See DOI: 10.1039/c9tc05550a

‡ Kyung Hyung Lee and Soon Ok Jeon contributed equally.

Synthesis

For the construction of **1PCTrz** and **2PCTrz** containing a phenyl substituted phenyl linker, an *N*-carbazolylcarbazole donor and a fluorophenyl modified diphenyltriazine group with one or two phenyl units were coupled by the S_NAr reaction as shown in Scheme 1. The fluoro intermediates were synthesized using a palladium catalyzed cross coupling procedure described in the ESI.† [26]

All three final products were purified by flash-column chromatography followed by sublimation to ensure >99.5% purity. The chemical structures were fully confirmed by the respective ^{1}H and ^{13}C NMR spectra and mass data. Their thermal properties were examined by thermogravimetric analysis (TGA) and differential scanning calorimetry (DSC) (see Fig. S1, ESI†). The decomposition temperature (T_d, corresponding to 5% weight loss) of **1PCTrz** and **2PCTrz** was similar to that of **CTrz**. Although the molecular weight was increased due to the attachment of one or two phenyl units, the temperature was not increased due to the twisted donor structure by attaching the phenyl subunits to the *ortho* positions of the phenyl linker. In the DSC measurements, both **CTrz** and **1PCTrz** exhibit a distinct glass-transition temperature (T_g) of 150 and 158 °C, respectively.

Calculations

The molecular geometries in the ground (S_0) state were optimized using the B3LYP[27] functional and the 6-31G(d,p) basis set. The excited-state geometries and energies were derived by time-dependent density functional theory (TD-DFT) at the MPW1B95[28]/6-31G(d,p) level of theory. The reverse intersystem crossing (RISC) rate, k_{RISC}, was computed by the Fermi Golden rule[29] and Marcus theory:[30,31]

$$k_{\mathrm{RISC}} = \frac{2\pi}{\hbar}|\langle S_1|H_{\mathrm{SO}}|T_1\rangle|^2\sqrt{\frac{1}{4\pi k_{\mathrm{B}}T\lambda_{\mathrm{S}}}}\exp\left[-\frac{(\Delta E_{\mathrm{ST}}+\lambda_{\mathrm{S}})^2}{4\lambda_{\mathrm{S}}k_{\mathrm{B}}T}\right]$$

where $|\langle S_1|H_{\mathrm{SO}}|T_1\rangle|$ is the Spin–Orbit Coupling (SOC) matrix element between the singlet excited state (S_1) and the triplet excited state (T_1). k_B is the Boltzmann constant and T is the temperature, which is set to 298 K. ΔE_{ST} denotes the energy difference between the S_1 and T_1 states, and λ_S represents the reorganization energy which can be formulated as:

$$\lambda_{\mathrm{S}} = E_{\mathrm{S1}}(\mathrm{T_1\ geometry}) - E_{\mathrm{S1}}(\mathrm{S_1\ geometry})$$

All the DFT and TD-DFT computations were performed using the Gaussian 09 package,[32] and the SOC calculations were performed using the ADF package.[33] The HONTO (Highest Occupied Natural Transition Orbital) and the LUNTO (Lowest Unoccupied Natural Transition Orbital) of S_1 and T_1 states were calculated by NANCY.[34,35] Also, we calculated the overlap between the HONTO and the LUNTO to describe CT (Charge-transfer) and LE (Local-excitation) characters for S1 and T1 states. The overlap between the HONTO and the LUNTO (Φ_s) was defined as

$$\Phi_{\mathrm{S}} = \frac{\int\sqrt{\rho_{\mathrm{H}}(r)\rho_{\mathrm{L}}(r)}\mathrm{d}r}{\frac{1}{2}\left[\int(\rho_{\mathrm{H}}(r)+\rho_{\mathrm{L}}(r))\mathrm{d}r\right]}$$

where $\rho_H(r)$ and $\rho_L(r)$ are the electronic densities of the HONTO and the LUNTO.

The calculation results are summarized in Table S1 (ESI†) to forecast the photophysical characteristics of the three emitters. The λ_S of the TADF emitters was decreased with the help of the phenyl subunits because they can restrict the molecular motion by steric hindrance. This can easily be predicted by the excited state geometry of the three emitters in S_1 and T_1 states in Fig. 1. The geometrical change in the S_1 and T_1 states was minimized in the **2PCTrz** emitter, which reduced the λ_S. The increase of the number of phenyl sub-units intensified the CT characters in both S_1 and T_1 states (Fig. 2). Although the three TADF emitters showed a small overlap value in the CT dominant S_1 state, the strengthened CT character of **1PCTrz** and **2PCTrz** in the S_1 state decreased the ΔE_{ST}. The large overlap value in the T_1 state of **CTrz** showed that the LE character is dominant in the T_1 state

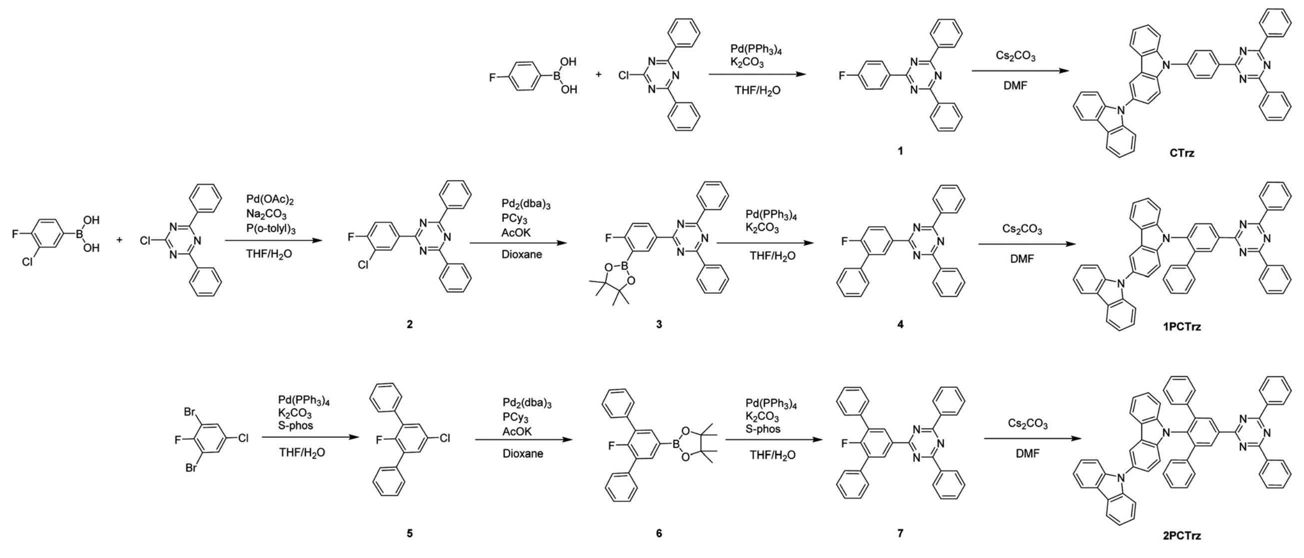

Scheme 1 Synthetic route to TADF materials.

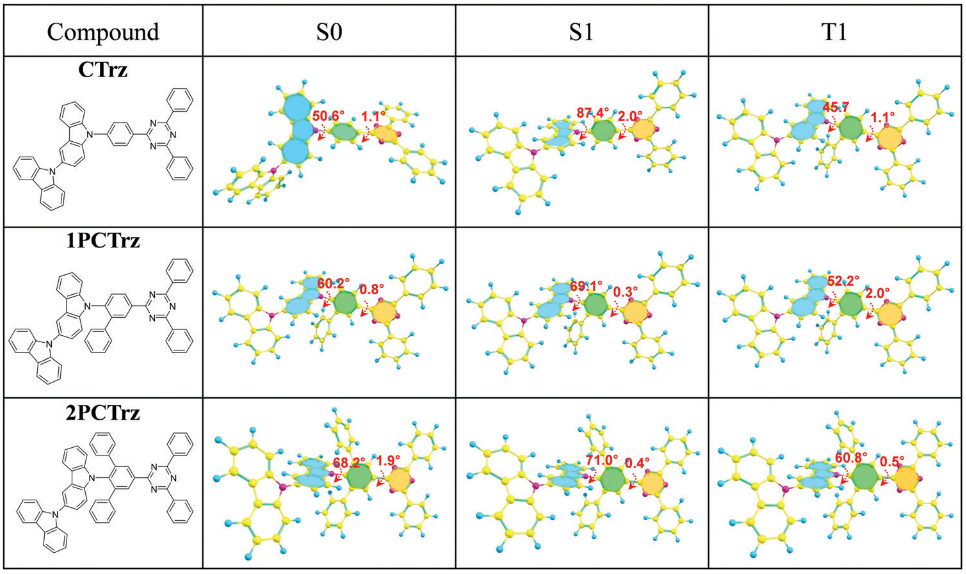

Fig. 1 Optimized geometry of the TADF emitters in the ground and excited states.

of **CTrz**. The dominant LE character in the T_1 state of **CTrz** improves the SOC matrix element value.[29]

The k_{RISC} values estimated from the calculated material parameters such as λ_S, the SOC matrix element, and ΔE_{ST} were gradually increased by adding the phenyl subunits. The SOC matrix element of **CTrz** is larger than those of two other emitters, but the reduction of ΔE_{ST} and λ_S was mostly responsible for the large k_{RISC} in **1PCTrz** and **2PCTrz** emitters. Therefore, the potential of the π-linker engineering method using phenyl subunits as a platform to improve the TADF characteristics of the emitters was confirmed.

The HOMO and LUMO levels of the TADF emitters were characterized by analyzing the ionization potential and electron affinity from the oxidation and reduction potentials of cyclic voltammetry measurements in Fig. S2 (ESI†). The estimated HOMO/LUMO levels of the **CTrz**, **1PCTrz**, and **2PCTrz** TADF

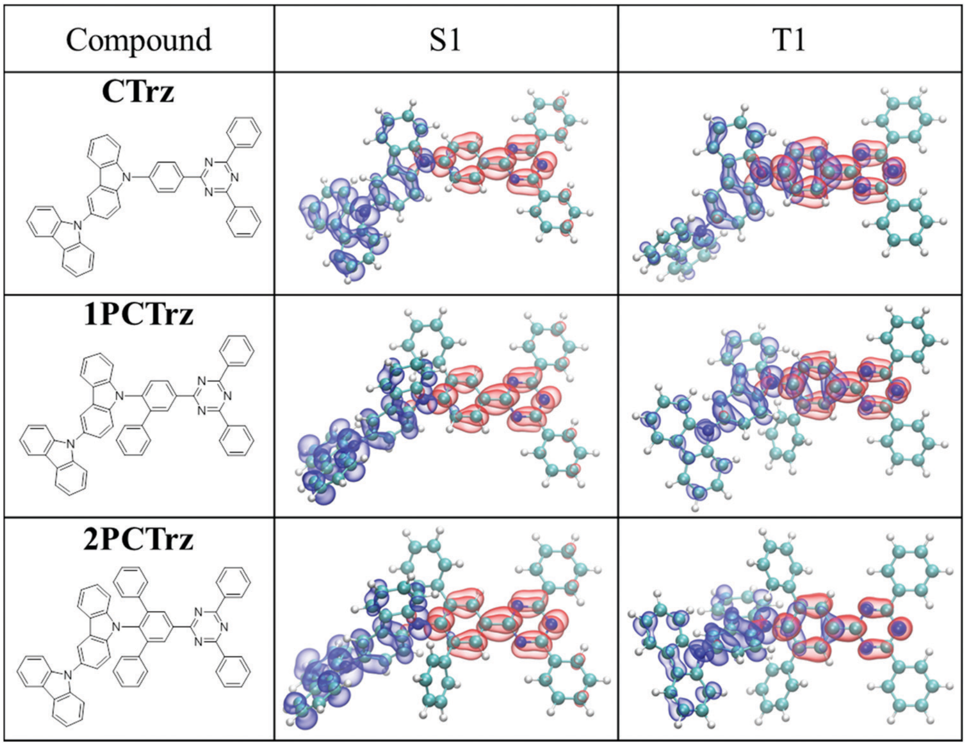

Fig. 2 HONTO (blue)/LUNTO(red) for the S_1 and T_1 states of TADF emitters.

emitters were −5.55/−2.55, −5.49/−2.51, and −5.50/−2.45 eV, respectively. The addition of a phenyl subunit had little effect on the energy levels although a slight HOMO level shift by the isolated donor unit was observed in the **1PCTrz** and **2PCTrz** emitters.

Photophysical properties

The photophysical characterization results of the TADF emitters are shown in Fig. 3. The singlet energy/triplet energy/ΔE_{ST} values of the **CTrz**, **1PCTrz**, and **2PCTrz** emitters were 3.13/2.89/0.24 eV, 3.06/2.90/0.16 eV and 2.97/2.86/0.11 eV, respectively, from the onset energy of the fluorescence and phosphorescence spectra. A gradual decrease of the singlet energy and ΔE_{ST} was noticed in the photoluminescence (PL) measurement of the emitters. As the fluorescence emission originated from CT emission as confirmed in the broad emission spectrum, the strong CT character of **1PCTrz** and **2PCTrz** stabilized the singlet energy. However, the triplet energy decrease was not as large as that of the singlet energy because the origin of phosphorescence is mixed emission of CT and local triplet emission. Although the CT character was strengthened by the phenyl subunits, the local triplet energy would be increased by the twisted structure disrupting the conjugation of the backbone structure, which resulted in a small change of the triplet energy. The simultaneous CT triplet energy reduction and local triplet energy increase hybridized the CT and local triplet excited states, resulting in the hybridized triplet excited states. This result was in agreement with the HONTO and LUNTO calculation results. The ΔE_{ST} was governed by the singlet energy as the triplet energy was similar to those of the three emitters. Therefore, the phenyl subunit was effective to reduce the ΔE_{ST}. In the ultraviolet-visible (UV-Vis) absorption, the main absorption in the backbone structure was similarly discerned and CT absorption below 400 nm was noted in the TADF emitters. The photophysical data are summarized in Table 1.

The dynamics of the TADF emission were analyzed using the transient PL characterization of the emitters doped in the DPEPO host. The prompt decay and delayed decay of the PL emission are presented in Fig. 4. The excited state lifetime for the prompt emission was relatively short in **CTrz** (11.6 ns) compared to those of **1PCTrz** (16.1 ns) and **2PCTrz** (29.3 ns). As the number of the phenyl subunits increased, the HOMO–LUMO overlap was reduced, which delayed the prompt emission process. However, the delayed fluorescence process was accelerated by the phenyl subunits. The delayed fluorescence lifetimes of **CTrz**, **1PCTrz**, and **2PCTrz** were 80.4, 55.8, and 31.4 μs, respectively. The strong CT character narrowing the gap between the singlet and triplet excited states facilitated the RISC process of the **1PCTrz** and **2PCTrz** TADF emitters. The RISC rate constants (k_{RISC}) were increased from 2.74×10^4 of **CTrz** to 3.97×10^4 of **1PCTrz** and 7.27×10^4 of **2PCTrz** (Table 2).

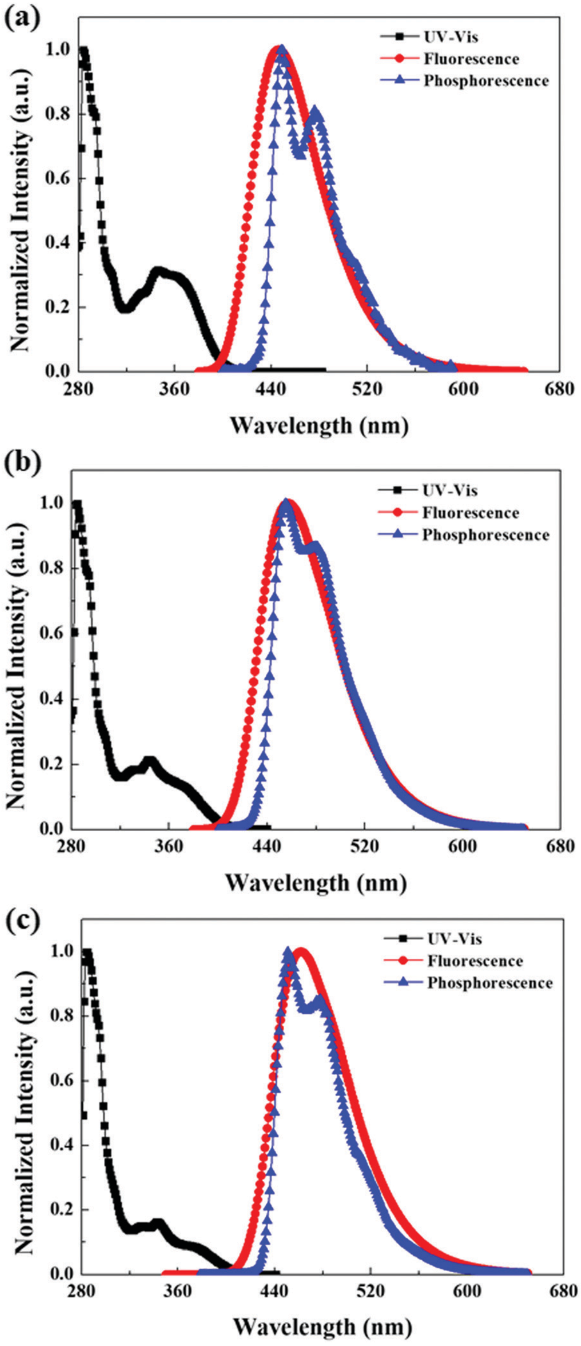

Fig. 3 UV-Vis and PL spectra of **CTrz** (a), **1PCTrz** (b) and **2PCTrz** (c) TADF emitters.

The PL quantum yield (PLQY) of the three TADF materials was measured by doping the emitter in the DPEPO host at an emitter content of 10 wt%. It was carried out to correlate the PLQY with the device performances of the TADF emitters by doping them into the DPEPO host at 10 wt% doping concentration. The PLQY under nitrogen was increased from 84% of **CTrz** to 87% of **1PCTrz** and 90% of **2PCTrz**. The phenyl subunits assisted the radiative transition of the TADF emitters along with the RISC process of the triplet excitons. The increased PLQY of the two TADF emitters built on the phenyl subunit platform is due to the reduction of the non-radiative transition as can be estimated from the non-radiative rate constants (k_{nr}) of 0.16×10^9 s^{-1}, 0.11×10^9 s^{-1} and 0.06×10^9 s^{-1} in **CTrz**, **1PCTrz** and **2PCTrz**, respectively.[36] The phenyl subunit seems to rigidify the backbone structure by applying large steric hindrance to the carbazolylcarbazole donor. In spite of the

Table 1 Summarized photophysical properties of **CTRz**, **1PCTRz** and **2PCTrz** TADF emitters

	HOMO[a] (eV)	LUMO[a] (eV)	HOMO–LUMO gap (eV)	Singlet energy[b] (eV)	Triplet energy[b] (eV)	ΔE_{ST} (eV)
CTrz	−5.55	−2.55	3.00	3.13	2.89	0.24
1PCTrz	−5.49	−2.51	2.98	3.06	2.90	0.16
2PCTrz	−5.50	−2.46	3.04	2.97	2.86	0.11

[a] Measured from cyclic voltammetry scanning. [b] Calculated from the fluorescent and phosphorescent spectrum onset point.

large distortion of the donor hampering the oscillator strength of the emitter by the isolated HOMO and LUMO, the suppressed non-radiative process positively influenced the PLQY of the emitters. This is well correlated with the small reorganization energy of **1PCTrz** and **2PCTrz** as summarized in Table S1 (ESI†).

Device performances

The TADF performances of the three emitters were evaluated in vacuum evaporated TADF devices by dispersing the TADF materials in the DPEPO host at a doping concentration of 20%. A high doping concentration was used to open a hole transport channel in the DPEPO host because the DPEPO is an electron transport type host with poor hole injection and transport properties. The device structure is shown in Fig. 5. The voltage sweep method was used to collect the current density (J) and luminance (L) data of TADF devices. The J and L plots of the TADF devices are presented in Fig. 6. The phenyl subunit in the π-linker affected the J of the TADF devices, resulting in low J values in **1PCTrz** and **2PCTrz** emitters. The reduction of J in the two devices can be interpreted by the effect of the phenyl subunit which twisted the carbazolylcarbazole donor from the phenyl linker. The carbazolylcarbazole donor was almost perpendicular to the phenyl linker, which hindered the carrier transport by a weak intermolecular orbital overlap for carrier hopping. The small twisting of the donor unit was advantageous for carrier hopping in the **CTrz** emitter. As the holes are mainly carried by the TADF emitters due to the large HOMO gap between the DPEPO and TADF emitters, the reduction of the hole transport properties by the subunits would be the main factor for the low J in **1PCTrz** and **2PCTrz.** In the case of L, the relative trend was the same as the J at low voltage, but the order of L disagreed with that of J at high voltage. This is due to external quantum efficiency (EQE) change according to L.

Table 2 Summarized PLQY and transient PL characteristics of **CTrz**, **1PCTrz** and **2PCTrz** TADF emitters

	Φ_{total}[a] (%)	Φ_{prompt} (%)	Φ_{TADF} (%)	τ_p (ns)	τ_d (μs)	k_{ISC}[b] (10^7 s^{-1})	k_{RISC}[b] (10^4 s^{-1})
CTrz	84	35	49	11.6	80.4	5.62	2.74
1PCTrz	87	36	51	16.1	55.8	3.99	3.97
2PCTrz	90	37	53	29.3	31.4	2.17	7.27

[a] 10 wt% doped film in DPEPO. [b] Calculated according to the method reported in ref. 37.

The EQE data of the TADF devices were plotted against current density in Fig. 7. The Lambertian distribution of light emission was assumed in the EQE measurement. The maximum EQE of the device was in the order of **2PCTrz** (28.5%) > **1PCTrz** (26.7%) > **CTrz** (24.8%). The maximum EQE was governed by the number of subunit in the phenyl linker. The increase of the number of subunits enhanced the maximum EQE of the TADF devices.

Considering the PLQY of the TADF emitters, the EQE of the TADF devices was rather high. Therefore, the horizontal dipole orientation of the emitters was measured by angle dependent PL analysis. The experimental results are presented in Fig. 8. The horizontal dipole orientation of the doped film was measured to correlate the device performances with the horizontal dipole orientation. The three doped emitters in the DPEPO matrix exhibited a horizontal dipole orientation ratio over 85%, suggesting that the three TADF emitters are similarly aligned along the substrate irrespective of the phenyl subunits. The anisotropic orientation of the dipole contributed to the high EQE of the three emitters. The EQE roll-off judged by the J value at which the EQE of the device is half of the maximum EQE followed the same order (**2PCTrz** (9.4 mA cm^{-2}) > **1PCTrz**

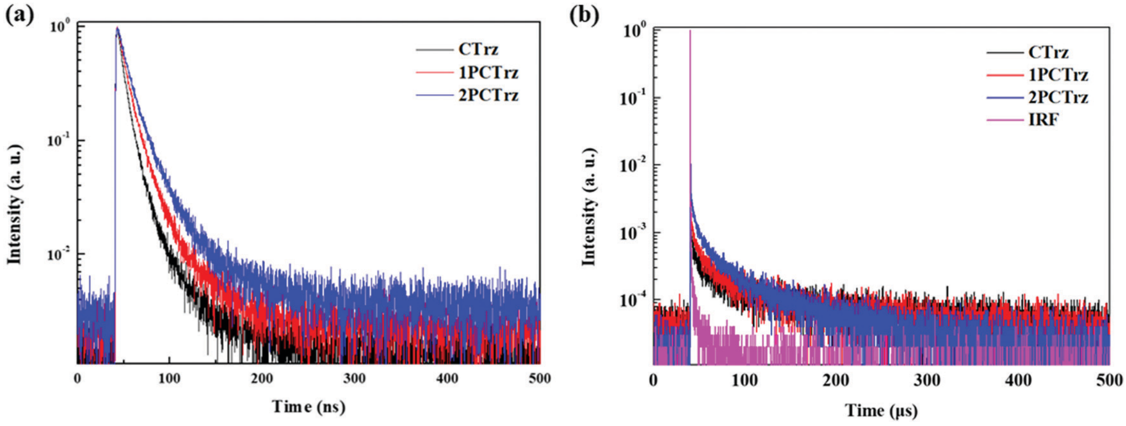

Fig. 4 The prompt decay (a) and delayed decay of (b) **CTrz**, **1PCTrz**, **2PCTrz** emitters doped in the DPEPO host at 10 wt% doping concentration and IRF (Instrument Response Function).

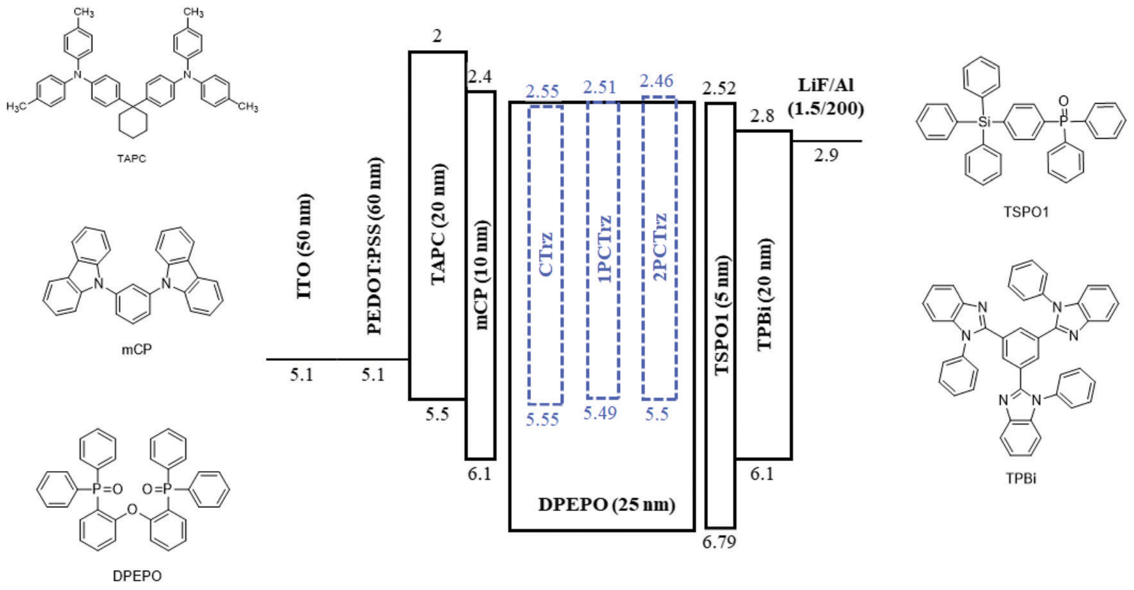

Fig. 5 Energy diagram of the TADF devices and chemical structure of the materials.

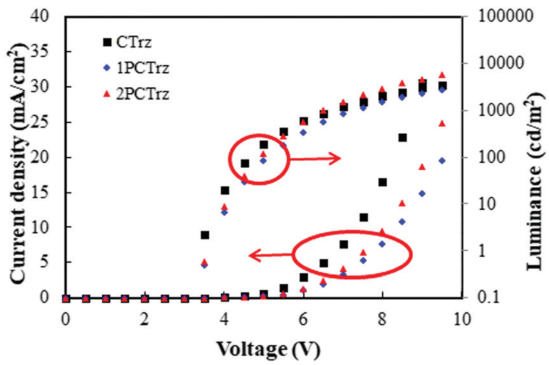

Fig. 6 The *J* and *L* plots of **CTrz**, **1PCTrz** and **2PCTrz** TADF devices.

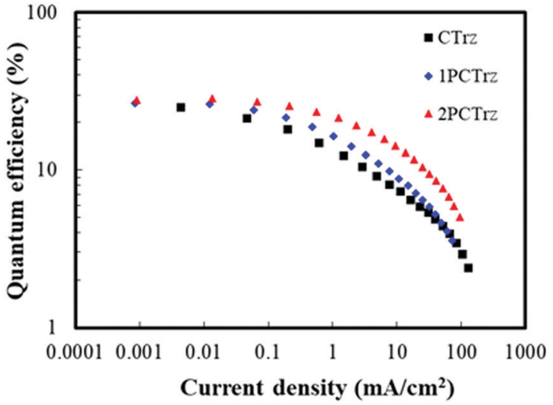

Fig. 7 The EQE data against current density of **CTrz**, **1PCTrz** and **2PCTrz** TADF devices.

(2.6 mA cm^{-2}) > **CTrz** (1.5 mA cm^{-2})) as the maximum EQE. The addition of the phenyl subunits improved the EQE roll-off characteristics of the TADF devices. As the EQE drop at high *L* is

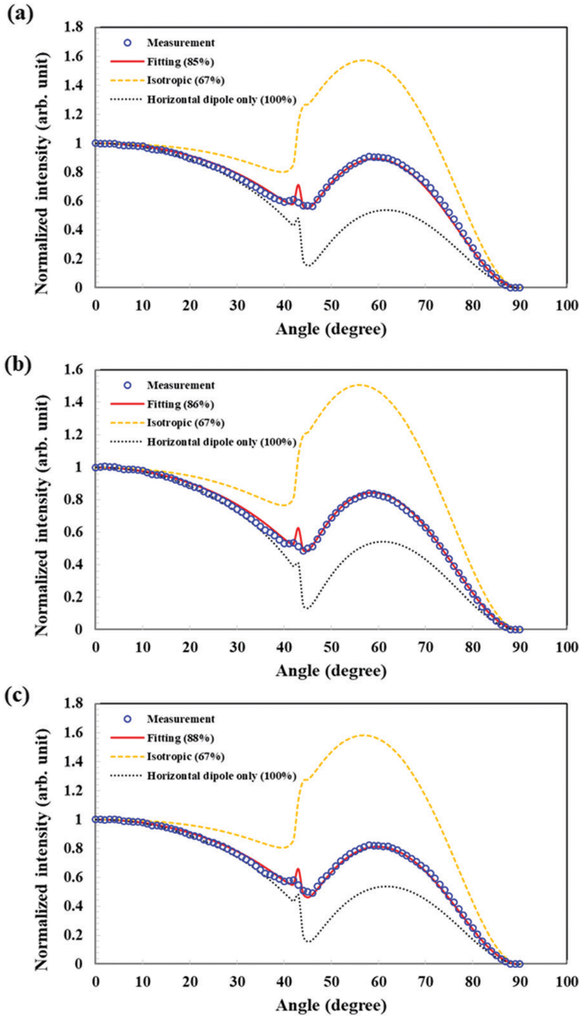

Fig. 8 The angle-dependent *p*-polarized PL intensity data of DPEPO:**CTrz** (a), DPEPO:**1PCTrz** (b) and DPEPO:**2PCTrz** (c).

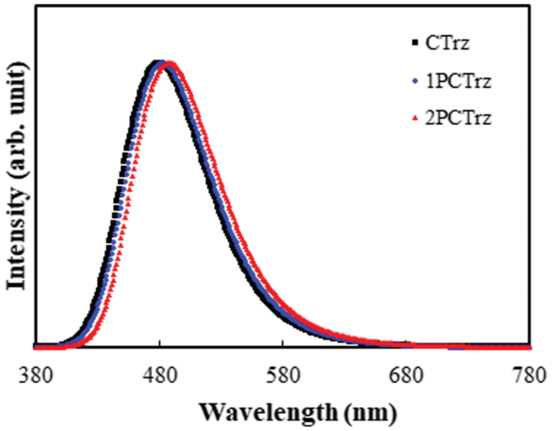

Fig. 9 The EL spectra of **CTrz**, **1PCTrz** and **2PCTrz** TADF devices.

triggered by the long excited state lifetime of triplet excitons, the reduced delayed fluorescence lifetime of the **1PCTrz** and **2PCTrz** emitters upgraded the EQE roll-off performances. The new blue TADF emitters with the phenyl subunit in the π-linker simultaneously improved the efficiency roll-off due to the facilitated RISC process and the suppressed non-radiative loss mechanism.

The light-emission spectra of the TADF devices in Fig. 9 show the emission spectra of **CTrz**, **1PCTrz** and **2PCTrz** TADF devices. The peak wavelengths of the **CTrz**, **1PCTrz**, and **2PCTrz** devices were 482, 482, and 488 nm, respectively. The corresponding color coordinates of the **CTrz**, **1PCTrz**, and **2PCTrz** devices were (0.17,0.28), (0.17,0.30), and (0.18, 0.35), respectively. The strong CT character of the **2PCTrz** by the twisted donor unit caused the bathochromic shift of the emission spectrum. The device data of the TADF devices are summarized in Table 3.

Conclusions

A molecular design platform to boost the external quantum efficiency and efficiency roll-off of the blue TADF emitters was developed by hiring one or two excited state controlling subunits in the π-linker between a donor and an acceptor. The phenyl subunit in the π-linker simultaneously improved the external quantum efficiency and efficiency roll-off of the TADF OLEDs due to the facilitated RISC process and the suppressed non-radiative loss mechanism. A high external quantum efficiency of 28.5% was achieved using the material design having two phenyl subunits in the blue emitters, opening a pathway to get access to the ideal device performances of blue TADF OLEDs.

Experimental

Chemicals were purchased from Sigma-Aldrich Co., Tokyo Chemical Industry Co., and Wako Pure Chemical Industries Ltd, and used without further purification. ^{1}H NMR and ^{13}C NMR spectra were recorded on a Bruker ASCEND 500 at 500 MHz using CD_2Cl_2 as the solvent. The MALDI-TOF mass spectra were recorded using a Bruker Ultraflex III TOF/TOF 200 spectrometer. The Ultraviolet-Visible (UV-Vis) spectra were obtained by means of a Varian model UV-Vis-NIR spectrophotometer 5000 and the fluorescence spectra were measured using a HITACHI F7000 spectrometer for the solution states. The UV-Vis absorption and solution photoluminescence (PL) emission spectra of the materials were obtained from dilute toluene solution (1×10^{-5} M), while the triplet energy values of the TADF materials were obtained from the photoluminescence spectra at 77 K using liquid nitrogen. The energy levels were measured by using cyclic voltammetry (CV). Each material was dissolved in anhydrous dichloromethane with 0.1 M tetrabutylammonium hexafluorophosphate as an electrolyte to measure the oxidation from which the HOMO energy level was estimated. Glassy carbon was used as the working electrode, a platinum wire was used as the counter electrode, and a saturated Ag/AgCl was used as the reference electrode. Ferrocene was used as the standard reference. All solutions were purged with nitrogen for 10 minutes before each experiment. The LUMO levels of each material were estimated from the difference between the HOMO energy level and the optical band gap which were estimated from the absorption edge of the UV-Vis spectra.

Synthesis

General procedure for S_NAr reaction: synthesis of 9-(4-(4,6-diphenyl-1,3,5-triazin-2-yl)phenyl)-9*H*-3,9′-bicarbazole (CTrz) as a representative. To a solution of 2-(4-fluorophenyl)-4,6-diphenyl-1,3,5-triazine (1.95 g, 5.96 mmol) in *N*,*N*-dimethylformamide (DMF, 20 mL) 9*H*-3,9′-bicarbazole (2.2 g, 6.62 mmol) and cesium carbonate (4.31 g, 13.24 mmol) were added at room temperature. The reaction mixture was stirred at 160 °C for 12 hours. After allowing it to cool to room temperature, the reaction mixture was diluted with MeOH (200 mL) and filtered. The reaction mixture was carefully washed with water/MeOH (100/100 mL). The resulting brown solid was collected by filtration. The crude product was purified by column chromatography using dichloromethane/*n*-hexane (1/3) as the eluent. The yellow solid was obtained and then the product was recrystallized from toluene and finally dried under vacuum to give 9-(4-(4,6-diphenyl-1,3,5-triazin-2-yl)phenyl)-9*H*-3,9′-bicarbazole (**CTrz**) as a yellow crystal in

Table 3 Summarized device performances of the **CTrz**, **1PCTrz** and **2PCTrz** devices

	External quantum efficiency (%)		Power efficiency (lm W^{-1})		Current efficiency (cd A^{-1})		Color coordinates	
	[1000 cd m^{-2}]	[Max]	[1000 cd m^{-2}]	[Max]	[1000 cd m^{-2}]	[Max]	x	y
CTrz	8.6	24.8	7.8	45.4	16.6	50.6	0.165	0.282
1PCTrz	11.7	26.7	10.2	50.2	23.5	55.9	0.171	0.302
2PCTrz	19.4	28.5	20.7	57.1	42.8	64.4	0.182	0.348

3.24 g (77%) yield. ^{1}H NMR (500 MHz, CD_2Cl_2): δ (ppm) 9.10 (d, 2H), 8.85 (d, 4H), 8.34 (s, 1H), 8.20 (d, 2H), 8.19 (d, 1H), 7.94 (d, 2H), 7.79 (d, 1H), 7.66 (m, 8H), 7.55 (t, 1H), 7.44 (m, 4H), 7.35 (t, 1H), 7.30 (m, 2H); ^{13}C NMR (75.5 MHz, CD_2Cl_2): 172.4, 171.49, 142.36, 141.74, 140.14, 136.70, 133.3, 131.29, 130.84,129.5, 129.31, 127.42, 127.35, 126.47, 126.41, 123.63, 121.34, 121.21, 120.75, 120.21, 119.99, 111.68, 110.88, 110.35; MALDI-TOF/MS: 639.34 [(M + H)$^+$]. Anal. calcd for $C_{45}H_{29}N_5$: C, 84.48; H, 4.57; N, 10.95. Found: C, 84.4; H, 4.6; N, 11.0.

9-(5-(4,6-Diphenyl-1,3,5-triazin-2-yl)-[1,1′-biphenyl]-2-yl)-9*H*-3,9′-bicarbazole (1PCTrz). By following the same procedure as that used for the synthesis of **CTrz**, using 2-(6-fluoro-[1,1′-biphenyl]-3-yl)-4,6-diphenyl-1,3,5-triazine (6.78 g, 16.85 mmol) as an acceptor and 9*H*-3,9′-bicarbazole (7.00 g, 21.06 mmol) as a donor **1PCTrz** (9.30 g, 62%) was synthesized. ^{1}H NMR (500 MHz, CD_2Cl_2): δ (ppm) 9.14 (d, 1H), 9.04 (dd, 1H), 8.84 (m, 4H), 8.22 (d, 1H), 8.18 (dd, 2H), 8.06 (d, 1H), 7.88 (d, 1H), 7.65 (m, 6H), 7.41 (m, 7H), 7.30 (m, 7H), 7.17 (m, 3H); ^{13}C-NMR (75.5 MHz, CD2Cl2): δ 170.91, 170.99, 141.79, 141.64, 141.22, 139.94, 138.51, 138.35, 136.95, 136.08, 132.78, 132.30, 129.99, 129.72, 129.40, 128.98, 128.75, 128.32, 128.05, 127.63, 126.53, 125.82, 125.24, 124.29, 123.00, 122.93, 120.40, 120.24, 120.13, 119.57, 119.16, 111.31, 110.43, 109.78; MALDI-TOF/MS: 715.37 [(M + H)$^+$]. Anal. calcd for $C_{51}H_{33}N_5$: C, 85.57; H, 4.65; N, 9.78. Found: C, 85.6; H, 4.6; N, 9.8.

9-(5′-(4,6-Diphenyl-1,3,5-triazin-2-yl)-[1,1′:3′,1″-terphenyl]-2′-yl)-9*H*-3,9′-bicarbazole (2PCTrz). By following the same procedure as that used for the synthesis of **CTrz**, using 2-(2′-fluoro-[1,1′:3′,1″-terphenyl]-5′-yl)-4,6-diphenyl-1,3,5-triazine (2.60 g, 5.41 mmol) as an acceptor and 9*H*-3,9′-bicarbazole (2.00 g, 6.02 mmol) as a donor **2PCTrz** (4.00 g, 84%) was synthesized. ^{1}H NMR (500 MHz, CD_2Cl_2): δ (ppm) 9.07 (s, 2H), 8.83 (dd, 4H), 8.16 (d, 2H), 8.04 (d, 1H), 7.91 (d, 1H), 7.65 (m, 2H), 7.61 (m, 4H), 7.41 (t, 2H), 7.33 (m, 5H), 7.29 (m, 6H), 7.13 (m, 8H); ^{13}C NMR (75.5 MHz, CD_2Cl_2): 172.6, 143.8, 142.4, 139.3, 136.6, 133.4, 131.7, 129.7, 129.4, 128.7, 128.1, 126.4, 125.6, 123.6, 120.7, 120.5, 120.1, 112.1, 111.2, 110.4; MALDI-TOF/MS: 791.40 [(M + H)$^+$]. Anal. calcd for $C_{57}H_{37}N_5$: C, 86.45; H, 4.71; N, 8.84. Found: C, 86.2; H, 4.7; N, 8.8.

Device fabrication and measurements

OLEDs were fabricated on indium-tin oxide (ITO) coated transparent glass substrates with an ITO conductive layer having a thickness of 50 nm. The active area of each device was 4 mm^2. The ITO glasses were ultrasonically cleaned using acetone and deionized water for 20 min. All organic functional layers and metal layers were deposited by the vacuum evaporation technique under a vacuum of 3×10^{-7} Torr. The device structure was ITO (50 nm)/poly(3,4-ethylenedioxythiophene):poly(styrenesulfonate) (PEDOT:PSS, 60 nm)/4,4′-cyclohexylidenebis[*N*,*N*-bis(4-methylphenyl)aniline] (TAPC, 20 nm)/1,3-bis(*N*-carbazolyl)benzene (mCP, 10 nm)/DPEPO:dopant (25 nm:20 wt%)/diphenylphosphine oxide-4-(triphenylsilyl)-phenyl (TSPO1, 5 nm)/2,2′,2″-(1,3,5-benzinetriyl)-tris(1-phenyl-1-*H*-benzimidazole) (TPBi) (40 nm)/LiF(1.5 nm)/Al(200 nm). The dopants were **CTrz**, **1PCTrz** and **2PCTrz**.

The material was thermally evaporated and then encapsulated with a glass lid in a nitrogen-filled glove box to protect the device from moisture and oxygen. Electrical characterization of the devices was performed using a Keithley 2400 source meter and optical characterization was carried out using a CS 2000 spectroradiometer.

Conflicts of interest

There are no conflicts to declare.

Acknowledgements

This material is based upon work supported in the part by the Samsung Advanced Institute of Technology (SAIT).

References

1 H. Uoyama, K. Goushi, K. Shizu, H. Nomura and C. Adachi, Highly efficient organic light-emitting diodes from delayed fluorescence, *Nature*, 2012, **492**, 234–238.

2 Y. R. Im, Y. J. Kim, Y. J. Cho, K. S. Seo., S. Yook and J. Y. Lee, Molecular Design Strategy of Organic Thermally Activated Delayed Fluorescence Emitters, *Chem. Mater.*, 2017, **29**, 1946–1963.

3 T. Hiroyuki, S. Katsuyuki, M. Hiroshi and C. Adachi, Efficient green thermally activated delayed fluorescence (TADF) from a phenoxazine–triphenyltriazine (PXZ–TRZ) derivative, *Chem. Commun.*, 2012, **48**, 11392–11394.

4 T. Furukawa, H. Nakanotani, M. Inoue and C. Adachi, Dual enhancement of electroluminescence efficiency and operational stability by rapid upconversion of triplet excitons in OLEDs, *Sci. Rep.*, 2015, **5**, 8429.

5 D. Zhang, L. Duan, C. Li, Y. Li, H. Li, D. Zhang and Y. Qui, High-Efficiency Fluorescent Organic Light-Emitting Devices Using Sensitizing Hosts with a Small Singlet–Triplet Exchange Energy, *Adv. Mater.*, 2014, **26**, 5050–5055.

6 V. Jankus, P. Data, D. Graves, C. McGuinness, J. Santos, M. R. Bryce, F. B. Dias and A. P. Monkman, Highly Efficient TADF OLEDs: How the Emitter–Host Interaction Controls Both the Excited State Species and Electrical Properties of the Devices to Achieve Near 100% Triplet Harvesting and High Efficiency, *Adv. Funct. Mater.*, 2014, **24**, 6178–6186.

7 D. Zhang, C. Zhao, Y. Zhang, X. Song, P. Wei, M. Cai and L. Duan, Highly Efficient Full-Color Thermally Activated Delayed Fluorescent Organic Light-Emitting Diodes: Extremely Low Efficiency Roll-Off Utilizing a Host with Small Singlet–Triplet Splitting, *ACS Appl. Mater. Interfaces*, 2017, **9**, 4769–4777.

8 D. R. Lee, B. S. Kim, C. W. Lee, Y. R. Im, K. S. Yook, S. H. Hwang and J. Y. Lee, Above 30% External Quantum Efficiency in Green Delayed Fluorescent Organic Light-Emitting Diodes, *ACS Appl. Mater. Interfaces*, 2015, **7**, 9625–9629.

9 Y. J. Cho, S. K. Jeon, B. D. Chin, E. S. Yu and J. Y. Lee, The Design of Dual Emitting Cores for Green Thermally

Activated Delayed Fluorescent Materials, *Angew. Chem.*, 2015, **54**, 5201–5204.

10 P. S. dos Santos, J. S. Ward, M. R. Bryce and A. P. Monkman, Using Guest–Host Interactions To Optimize the Efficiency of TADF OLEDs, *J. Phys. Chem. Lett.*, 2016, **7**, 3341–3346.

11 B. S. Kim and J. Y. Lee, Engineering of Mixed Host for High External Quantum Efficiency above 25% in Green Thermally Activated Delayed Fluorescence Device, *Adv. Funct. Mater.*, 2014, **24**, 3970–3977.

12 M. G. Kim, S. K. Jeon, S. H. Hwang and J. Y. Lee, Stable Blue Thermally Activated Delayed Fluorescent Organic Light-Emitting Diodes with Three Times Longer Lifetime than Phosphorescent Organic Light-Emitting Diodes, *Adv. Mater.*, 2015, **27**, 2515–2520.

13 J. Gibson, A. P. Monkman and T. J. Penfold, The Importance of Vibronic Coupling for Efficient Reverse Intersystem Crossing in Thermally Activated Delayed Fluorescence Molecules, *ChemPhysChem*, 2016, **17**, 2956–2961.

14 Q. Zhang, B. Li, S. Huang, H. Nomura, H. Tanaka and C. Adachi, Efficient blue organic light-emitting diodes employing thermally activated delayed fluorescence, *Nat. Photonics*, 2014, **8**, 326–332.

15 W. X. Zeng, H. Y. Lai, W. K. Lee, M. Jiao, Y. J. Shiu, C. Zhong, S. L. Gong, T. Zhou, G. Xie, M. Sarma, K. T. Wong, C. C. Wu and C. Yang, Achieving Nearly 30% External Quantum Efficiency for Orange–Red Organic Light Emitting Diodes by Employing Thermally Activated Delayed Fluorescence Emitters Composed of 1,8-Naphthalimide-Acridine Hybrids, *Adv. Mater.*, 2018, **30**, 1704961.

16 R. Braveenth, H. Lee, S. Kim, K. Raagulan, S. Kim, J. H. Kwon and K. Y. Chai, High efficiency green TADF emitters of acridine donor and triazine acceptor D–A–D structures, *J. Mater. Chem. C*, 2019, **7**, 7672–7680.

17 W. Li, B. B. Li, X. Y. Cai, L. Gan, Z. D. Xu, W. Q. Li, K. K. Liu, D. C. Chen and S. J. Su, Tri-Spiral Donor for High Efficiency and Versatile Blue Thermally Activated Delayed Fluorescence Materials, *Angew. Chem., Int. Ed.*, 2019, **58**, 11301–11305.

18 W. Zeng, T. Zhou, W. Ning, C. Zhong, J. He, S. Gong, G. Xie and C. Yang, Realizing 22.5% External Quantum Efficiency for Solution-Processed Thermally Activated Delayed-Fluorescence OLEDs with Red Emission at 622 nm via a Synergistic Strategy of Molecular Engineering and Host Selection, *Adv. Mater.*, 2019, **31**, 1901404.

19 S. J. Woo, Y. H. Kim, S. K. Kwon, Y. H. Kim and J. J. Kim, Phenazasiline/Spiroacridine Donor Combined with Methyl-Substituted Linkers for Efficient Deep Blue Thermally Activated Delayed Fluorescence Emitters, *ACS Appl. Mater. Interfaces*, 2019, **11**, 7199–7207.

20 L. S. Cui, H. Nomura, Y. Geng, J. U. Kim, H. Nakanotani and C. Adachi, Controlling Singlet–Triplet Energy Splitting for Deep-Blue Thermally Activated Delayed Fluorescence Emitters, *Angew. Chem., Int. Ed.*, 2017, **56**, 1571–1575.

21 K. C. Pan, S. W. Li, Y. Y. Ho, Y. J. Shiu, W. L. Tsai, M. Jiao, W. K. Lee, C. C. Wu, C. L. Chung, T. Chatterjee, Y. S. Li, K. T. Wong, H. C. Hu, C. C. Chen and M. T. Lee, Efficient and Tunable Thermally Activated Delayed Fluorescence Emitters Having Orientation-Adjustable CN-Substituted Pyridine and Pyrimidine Acceptor Units, *Adv. Funct. Mater.*, 2016, **26**, 7560–7571.

22 W. Liu, C. J. Zheng, K. Wang, Z. Chen, D. Y. Chen, F. Li, X. M. Ou, Y. P. Dong and X. H. Zhang, Novel Carbazol-Pyridine-Carbonitrile Derivative as Excellent Blue Thermally Activated Delayed Fluorescence Emitter for Highly Efficient Organic Light-Emitting Devices, *ACS Appl. Mater. Interfaces*, 2015, **7**, 18930–18936.

23 D. R. Lee, S. H. Han, C. W. Lee and J. Y. Lee, Bis(diphenyltriazine) as a new acceptor of efficient thermally activated delayed fluorescent emitters, *Dyes Pigm.*, 2018, **151**, 75–80.

24 M. G. Kim, J. M. Choi and J. Y. Lee, Simultaneous improvement of emission color, singlet–triplet energy gap, and quantum efficiency of blue thermally activated delayed fluorescent emitters using a 1-carbazolylcarbazole based donor, *Chem. Commun.*, 2016, **52**, 10032–10035.

25 S. Hirata, Y. Sakai, K. Masui, H. Tanaka, S. Y. Lee, H. Nomura, N. Nakamura, M. Yasumatsu, H. Nakanotani and Q. Zhang, Highly efficient blue electroluminescence based on thermally activated delayed fluorescence, *Nat. Mater.*, 2015, **14**, 330–336.

26 S. Kozuch and J. M. L. Martin, What makes for a good catalytic cycle? A theoretical study of the SPhos ligand in the Suzuki–Miyaura reaction, *Chem. Commun.*, 2011, **47**, 4935–4937.

27 P. J. Stephens, F. J. Devlin, C. F. Chabalowski and M. J. Frisch, Ab initio calculation of vibrational absorption and circular dichroism spectra using density functional force fields, *J. Phys. Chem.*, 1994, **98**, 11623–11627.

28 Y. Zhao and D. G. Truhlar, hybrid meta density functional theory methods for thermochemistry, thermochemical kinetics, and noncovalent interactions: the MPW1B95 and MPWB1K models and comparative assessments for hydrogen bonding and van der Waals interactions, *J. Phys. Chem. A*, 2004, **108**, 6908–6918.

29 P. K. Samanta, D. Kim, V. Coropceanu and J.-L. Bredas, Up-Conversion intersystem crossing rates in organic emitters for thermally activated delayed fluorescence: Impact of the nature of singlet vs triplet excited states, *J. Am. Chem. Soc.*, 2017, **139**, 4042–4051.

30 R. A. Marcus, On the Theory of Oxidation-Reduction Reactions Involving Electron Transfer, *J. Chem. Phys.*, 1956, **24**, 966–978.

31 S. Feng, K. Wen, Y. Si, X. Guo and J. Zhang, Theoretical studies on thermally activated delayed fluorescence mechanism of a series of organic light-emitting diodes emitters comprising 2,7-diphenylamino-9,9-dimethylacridine as electron donor, *J. Comput. Chem.*, 2018, **39**, 2601–2606.

32 M. J. Frisch, G. W. Trucks, H. B. Schlegel, G. E. Scuseria, M. A. Robb, J. R. Cheeseman, G. Scalmani, V. Barone, B. Mennucci, G. A. Petersson, H. Nakatsuji, M. Caricato, X. Li, H. P. Hratchian, A. F. Izmaylov, J. Bloino, G. Zheng, J. L. Sonnenberg, M. Hada, M. Ehara, K. Toyota, R. Fukuda, J. Hasegawa, M. Ishida, T. Nakajima, Y. Honda, O. Kitao, H. Nakai, T. Vreven, J. A. Montgomery Jr., J. E. Peralta, F. Ogliaro, M. Bearpark, J. J. Heyd, E. Brothers, K. N. Kudin,

V. N. Staroverov, R. Kobayashi, J. Normand, K. Raghavachari, A. Rendell, J. C. Burant, S. S. Iyengar, J. Tomasi, M. Cossi, N. Rega, J. M. Millam, M. Klene, J. E. Knox, J. B. Cross, V. Bakken, C. Adamo, J. Jaramillo, R. Gomperts, R. E. Stratmann, O. Yazyev, A. J. Austin, R. Cammi, C. Pomelli, J. W. Ochterski, R. L. Martin, K. Morokuma, V. G. Zakrzewski, G. A. Voth, P. Salvador, J. J. Dannenberg, S. Dapprich, A. D. Daniels, Ö. Farkas, J. B. Foresman, J. V. Ortiz, J. Cioslowski and D. J. Fox, *Gaussian 09, Revision E.01*, Gaussian, Inc., Wallingford CT, 2009.

33 ADF2016, SCM, Theoretical Chemistry, Vrije Universiteit, Amsterdam, The Netherlands, http://www.scm.com. Optionally, you may add the following list of authors and contributors: E. J. Baerends, T. Ziegler, A. J. Atkins, J. Autschbach, D. Bashford, A. Bérces, F. M. Bickelhaupt, C. Bo, P. M. Boerrigter, L. Cavallo, D. P. Chong, D. V. Chulhai, L. Deng, R. M. Dickson, J. M. Dieterich, D. E. Ellis, M. van Faassen, L. Fan, T. H. Fischer, C. Fonseca Guerra, M. Franchini, A. Ghysels, A. Giammona, S. J. A. van Gisbergen, A. W. Götz, J. A. Groeneveld, O. V. Gritsenko, M. Grüning, S. Gusarov, F. E. Harris, P. van den Hoek, C. R. Jacob, H. Jacobsen, L. Jensen, J. W. Kaminski, G. van Kessel, F. Kootstra, A. Kovalenko, M. V. Krykunov, E. van Lenthe, D. A. McCormack, A. Michalak, M. Mitoraj, S. M. Morton, J. Neugebauer, V. P. Nicu, L. Noodleman, V. P. Osinga, S. Patchkovskii, M. Pavanello, C. A. Peeples, P. H. T. Philipsen, D. Post, C. C. Pye, W. Ravenek, J. I. Rodríguez, P. Ros, R. Rüger, P. R. T. Schipper, H. van Schoot, G. Schreckenbach, J. S. Seldenthuis, M. Seth, J. G. Snijders, M. Solà, M. Swart, D. Swerhone, G. te Velde, P. Vernooijs, L. Versluis, L. Visscher, O. Visser, F. Wang, T. A. Wesolowski, E. M. van Wezenbeek, G. Wiesenekker, S. K. Wolff, T. K. Woo and A. L. Yakovlev.

34 T. Etienne, X. Assfeld and A. Monari, Toward a Quantitative Assessment of Electronic Transitions' Charge-Transfer Character, *J. Chem. Theory Comput.*, 2014, **10**, 3896–3905.

35 T. Etienne, X. Assfeld and A. Monari, New Insight into the Topology of Excited States through Detachment/Attachment Density Matrices-Based Centroids of Charge, *J. Chem. Theory Comput.*, 2014, **10**, 3906–3914.

36 V. V. N. Ravi Kishore, K. L. Narasimhan and N. Periasamy, On the radiative lifetime, quantum yield and fluorescence decay of Alq in thin films, *Phys. Chem. Chem. Phys.*, 2003, **5**, 1386–1391.

37 K. Masui, H. Nakanotani and C. Adachi, Analysis of exciton annihilation in high-efficiency sky-blue organic light-emitting diodes with thermally activated delayed fluorescence, *Org. Electron.*, 2013, **14**, 2721–2726.